Nonhydrolytic Synthesis and Electronic Structure of Ligand-Capped $CeO_{2-\delta}$ and CeOCl Nanocrystals

Sean W. Depner,[†] Kenneth R. Kort,[†] Cherno Jaye,[‡] Daniel A. Fischer,[‡] and Sarbajit Banerjee*,[†]

Department of Chemistry, University at Buffalo, State University of New York, Buffalo, New York 14260-3000, and Materials Science and Engineering Laboratory, National Institute of Standards and Technology, Gaithersburg, Maryland 20899

Received: April 7, 2009; Revised Manuscript Received: June 10, 2009

A novel and versatile nonhydrolytic approach is developed for the synthesis of ligand-passivated $CeO_{2-\delta}$ and CeOCl nanocrystals soluble in nonpolar organic solvents based on the condensation of cerium alkoxides with cerium halides. The alkyl group on the metal alkoxides and the specific halide used in the synthesis are observed to considerably influence the composition and size of the obtained nanocrystals. The obtained nanocrystals are <3 nm in diameter and, owing to their surface-capping groups, yield homogeneous and clear solutions in nonpolar organic solvents with no evidence of agglomeration. The electronic structure of the obtained $CeO_{2-\delta}$ nanocrystals has been studied using optical absorption spectroscopy and near-edge X-ray absorption fine structure spectroscopy at Ce M- and O K-edges. The latter technique provides detailed insight into the metal valence, geometric structure, and atom-projected density of states in these nanocrystals. Finally, this synthesis method has been expanded to explore the doping of La to form solid-solution $Ce_xLa_{1-x}O_{2-\delta}$ nanocrystals.

Introduction

Significant progress has been achieved over the past decade in understanding the influence of finite size on material properties spurred largely by the development of synthetic methodologies for the fabrication of nanostructures with controlled dimensionality, morphology, and surface chemistry.[1,2] Groups II−VI chalcogenide semiconductor nanocrystals represent particularly well-developed examples of materials that have benefited greatly from advances in hot colloidal synthesis methods, especially the separation of nucleation and growth steps.[3,4] These materials are now rapidly approaching commercialization in no small measure because of the availability of robust and reproducible synthetic approaches that yield monodisperse nanocrystals with considerable control over size, shape, and surface chemistry. Scaling the rare earth oxide, cerium oxide, CeO_2, to nanoscale dimensions has attracted tremendous attention over the past decade because of its remarkable optical, redox, and mechanical properties, which leads to a diverse range of technological applications, for example, in three-way catalysts for treating automotive exhaust,[5] as a strong UV light absorber and shielding material in the harmful 210−310 nm region for use in sunscreen cosmetics and window materials,[6] as an electrolyte in solid oxide fuel cells (SOFCs),[7,8] as a superionic conductor and oxygen gas sensor,[9] as the most widely used abrasive for the chemical−mechanical polishing of precise optics,[10] and as a high k gate dielectric layer on Si[11] or a buffer layer for high-T_c thin-film superconductors.[12] This remarkably diverse array of applications for CeO_2 arises from its high dielectric constant, the facile reversibility of the Ce^{3+}/Ce^{4+} redox couple, the related excellent tolerance of the fluorite structure to high concentrations of dopants and oxygen vacancies, and the characteristic strong ligand-to-metal charge transfer absorption band in the ultraviolet region of the electromagnetic spectrum.[13] Several of these properties are expected to show considerable size tunability.[6,14] For example, it has recently been shown that nanocrystalline CeO_2 increases the activity of supported gold catalysts toward CO oxidation by 2 orders of magnitude.[15] The origin of the increased catalytic activity is thought to be the stabilization of reactive oxygen species on the ceria support and the optimization of the catalyst/support interface.[15] Gold clusters supported on nanocrystalline ceria are also one of the most active catalysts for the water−gas shift (WGS) reaction ($CO + H_2O \leftrightarrow CO_2 + H_2$), which has attracted much renewed interest as a means of generating/purifying H_2 for fuel cells.[16,17] The potential for increased tunability of desirable optical, catalytic, and redox properties has fuelled an extensive research effort focused on the preparation of nanostructured ceria with controlled size, shape, and surface chemistry.

Several approaches have been reported for the synthesis of nanocrystalline CeO_2, including from a colloidal dispersion,[15] alcohothermal and hydrothermal synthesis,[18] the polyol method,[19a] sonochemical methods,[20] arrested precipitation,[21−23] and the thermolysis of organometallic precursors.[24,25] Considerable control has been established over the size, shape, and crystallographic growth direction of CeO_2 nanostructures. For example, Mai et al. have used a hydrothermal approach to prepare CeO_2 nanopolyhedra, nanorods, and nanocubes bound by different crystallographic facets.[19b] Remarkably, Si and Flytzani-Stephanopoulos have shown that these differently shaped CeO_2 nanostructures show starkly different reactivity in the water−gas shift reaction catalyzed by CeO_2-supported nanocrystalline gold catalysts.[26] However, the vast majority of synthetic efforts for the preparation of CeO_2 nanocrystals reported thus far is aqueous-based, typically yielding agglomer-

* To whom correspondence should be addressed. E-mail: sb244@buffalo.edu.
[†] University at Buffalo, State University of New York.
[‡] National Institute of Standards and Technology.

10.1021/jp903216b CCC: $40.75
Published on Web 07/15/2009

ated nanocrystals with hydroxylated surfaces. CeO_2 nanocrystals obtained using such approaches exhibit very limited dispersibility in organic or aqueous media and, in general, do not have a well-characterized surface chemistry. In this regard, the synthesis of CeO_2 nanocrystals is not as well developed as that of groups II−VI chalcogenide quantum dots wherein the nanocrystal surfaces are passivated by (typically hydrophobic) ligand molecules that prevent agglomeration and impart solubility in organic and aqueous media.[2,4] The colloidal synthesis of nanocrystals in high-boiling-point organic solvents in the presence of passivating ligands typically yields nanocrystals with far better monodispersity, crystallinity, and tunable surface chemistry as compared with those of comparable aqueous approaches.[27] The presence of passivating ligands imparts solubility in different solvents and, coupled with the development of ligand-exchange protocols, enables the formation of nanocomposites based on the dispersion of nanocrystals within polymer matrices. Relatively little attention has been devoted to the hot colloidal synthesis of CeO_2 nanocrystals in organic solvents. Si et al. have briefly noted that the decomposition of a cerium(IV) benzylacetone complex in a mixture of oleic acid and oleylamine at 250 °C yields CeO_2 nanopolyhedra with a diameter of 2.6 nm.[24] An analogous approach based on the decomposition of cerium−oleate complexes in different high-boiling-point organic solvents has been used to prepare monodisperse CeO_2 nanocrystals with diameters ranging from 5 to 20 nm.[25] In contrast, several nonhydrolytic synthesis approaches based on the decomposition of metal acetates and metal oleates or the nonhydrolytic sol−gel condensation of metal halides with metal alkoxides have been developed for the fabrication of high-quality ligand-capped nanocrystals of other early transition-metal oxides, such as TiO_2, ZrO_2, and HfO_2.[28−32] In a prominent example, Hyeon and co-workers have prepared 4 nm diameter tetragonal zirconia nanoparticles soluble in nonpolar solvents by a modified nonhydrolytic sol−gel condensation method originally used to prepare TiO_2 nanocrystals.[29,32] This synthetic approach is based on the formation of M−O−M bonds by the condensation of a metal alkoxide with a metal chloride with the elimination of an alkyl halide as per

$$\equiv M-X + \equiv M-O-R \rightarrow \equiv M-O-M\equiv + R-X \tag{1}$$

Brus, Steigerwald, and co-workers have extended this synthetic approach to prepare solid-solution $Hf_xZr_{1-x}O_2$ nanocrystals based on the heterocondensation reaction[30,31]

$$m\mathrm{MX}_n + n\mathrm{M}'(\mathrm{OR})_m \rightarrow \mathrm{M}_m\mathrm{M}'_n\mathrm{O}_{nm} + nm\mathrm{RX} \tag{2}$$

between hafnium halides and zirconium alkoxides or between zirconium halides and hafnium alkoxides. In some recent work, we have demonstrated that the alkyl group in the metal alkoxide precursor exerts a very profound influence on the crystal structure and composition of twin metal oxide $Hf_xZr_{1-x}O_2$ nanocrystals obtained by this nonhydrolytic heterocondensation method.[33] Remarkably, linear or secondary alkoxide precursors yield tetragonal $Hf_xZr_{1-x}O_2$ nanocrystals, whereas *tert*-butyl alkoxides yield the monoclinic polymorph for the same $Hf_xZr_{1-x}O_2$ composition.

Here, we illustrate a versatile strategy for the synthesis of ligand-capped $CeO_{2-\delta}$ and CeOCl nanocrystals soluble in nonpolar solvents based on the nonhydrolytic condensation of cerium alkoxides with cerium halides. Considerable tunability of nanocrystal composition and size has been achieved by varying the alkyl group in the cerium alkoxide and the halide species in the cerium halide. The heterocondensation approach noted in eq 2 also allows the facile incorporation of La^{3+} ions in the $CeO_{2-\delta}$ lattice. As discussed in more detail below, the use of Ce(III) halides results in the introduction of a high concentration of oxygen vacancies in the obtained nanocrystals. Optical absorption spectroscopy measurements, in combination with near-edge X-ray absorption fine structure (NEXAFS) spectroscopy measurements at the O K-edge and the Ce M-edge, have been used to obtain a comprehensive understanding of the electronic structure of the obtained $CeO_{2-\delta}$ nanocrystals. The key advantage offered by this approach is the ligand passivation of the CeO_2 surfaces, which prevents agglomeration and engenders facile dispersibility in nonpolar solvents. Such organic-soluble $CeO_{2-\delta}$ nanocrystals are expected to be useful building blocks for the formation of hybrid inorganic−organic nanocomposites. The availability of various efficacious ligand-exchange protocols for swapping TOPO ligands with other hydrophobic or hydrophilic ligands while still retaining nanoparticle dispersion paves the way for the fabrication of multifunctional CeO_2 nanocomposites.

Experimental Section

Synthesis. Tri-*n*-octylphosphine oxide (TOPO, 90%), cerium(III) chloride (99.9%), and lanthanum(III) chloride (99.9%) were purchased from Strem and used as received. Cerium(III) bromide (99.9%) and cerium(III) iodide (99.9%) were purchased from Sigma-Aldrich, cerium(IV) *tert*-butoxide was purchased from Gelest, cerium(IV) isopropoxide was purchased from Alfa Aesar, and lanthanum(III) isopropoxide (98%) was obtained from Acros Organics. The general reaction procedure involved the addition of 2 mmol of the metal alkoxide to 2 mmol of the metal halide and 10 g of degassed TOPO in a three-neck reaction vessel within an Ar-filled glovebox. The cerium and lanthanum alkoxides are moisture-sensitive, and thus, considerable care is exercised to make sure that they are not exposed to the ambient atmosphere. The reaction mixture was first heated to ∼60 °C to allow the TOPO to melt under an argon atmosphere using a standard Schlenk setup. Next, stirring was initiated and the temperature was raised to 325 °C, and the reaction mixture was maintained at this temperature for 1 h. Subsequently, the reaction was cooled to ∼60 °C and acetone was added to flocculate the formed nanocrystals. The nanocrystals were recovered by centrifugation at 12 000 rpm for 25 min and were then redispersed in hexane. A second centrifugation was performed at 1500 rpm for 5 min to remove insoluble impurities (including unreacted precursors and some oxychloride products, as noted below), and the dissolved nanocrystals were again flocculated by the addition of acetone. Products thus isolated were observed to be phase-pure within the limits of detection of X-ray diffraction and Raman spectroscopy.

Characterization. A Siemens D-500 instrument was used to acquire X-ray diffraction (XRD) data using Cu Kα radiation (1.5418 Å). High-resolution transmission electron microscopy (HRTEM) images were obtained using a JEOL 2010 instrument operating at 200 kV. Initial low-resolution transmission electron microscopy images were acquired using a JEOL 100CX instrument at an accelerating voltage of 100 kV. Optical absorption spectra were collected in the range from 190 to 820 nm on a Hewlett-Packard 8452A diode array spectrophotometer. The nanocrystal samples were dissolved in hexane, and a quartz cell with a 1 cm path length was used for these measurements. Fourier transform infrared (FTIR) spectroscopy measurements were performed using a Nicolet Magna 550 instrument in transmission mode for KBr pellets mixed with the nanocrystals. Raman measurements of powder samples were performed using a Horiba Jobin-Yvon LabRamHR single spectrometer instrument with an edge filter for rejection of the Rayleigh line and a Peltier-cooled CCD camera from Andor. Raman spectra for the $CeO_{2-\delta}$ nanocrystals were acquired using 784.5 nm laser excitation to avoid fluorescence. Raman spectra for CeOCl and LaOCl samples were acquired using the 514.5 nm excitation from an Ar^+ laser. Inductively coupled plasma optical emission spectroscopy (ICP-OES) measurements were performed at Columbia Analytical Services, Tucson, AZ. NEXAFS measurements were preformed at the National Institute of Standards and Technology beamline U7A at the National Synchrotron Light Source at Brookhaven National Laboratory. A toroidal mirror spherical grating monochromator using a 1200 lines/mm grating with a nominal energy resolution of ~0.1 eV was used to disperse the incident soft X-rays. A Channeltron electron multiplier detector located near the sample was used to record the spectra with an entrance grid bias of −200 V to enhance surface sensitivity. A charge compensation electron gun was used to avoid charging effects for the insulating samples. O K-edge and second harmonic Ce M-edge spectra were acquired using metallic vanadium and NiCoFeCr meshes, respectively, as standards for energy calibration of each individual spectrum. To eliminate the effects of fluctuations in the incident beam intensity and monochromator absorption features, the drain current of a freshly evaporated gold mesh with 90% transmittance located along the path of the incident X-rays was used to normalize the partial electron yield signals. All data were collected at magic-angle ($\theta = 54.7°$) incidence of the X-ray beam.

Results and Discussion

On the basis of observations for analogous lower-temperature reactions yielding metal oxides, the nonhydrolytic condensation of the metal halide and metal alkoxide depicted in eq 1 is thought to proceed via the initial complexation of the alkoxide oxygen to the metal center on the metal halide.[29,34] Subsequently, the O−R bond in the alkoxide is cleaved by the nucleophilic attack of the halide at the alkoxide carbon, resulting in the elimination of the alkyl halide. This step is thought to be the rate-limiting step controlling the nucleation and growth of the metal oxide nanocrystal products.[29] An S_N1 mechanism has been proposed for the nucleophilic attack of the halide at the alkoxide carbon, and thus, electronic effects at the carbon are likely to exert a strong influence on the reaction rate.[29,34] Indeed, Colvin and co-workers have observed dramatically increased reaction rates for the reaction of titanium alkoxides with titanium halides (yielding TiO_2 nanocrystals) as the degree of branching of the alkoxides is increased and carbocation formation becomes easier.[29] As noted above, we have recently observed that *tert*-butyl metal alkoxides yield monoclinic solid-solution $Hf_xZr_{1-x}O_2$ nanocrystals, whereas their primary and secondary metal alkoxide counterparts yield the tetragonal polymorph with the same chemical composition. This dramatic difference in reactivity is thought to arise from the starkly different reaction rates for the different alkoxides; the *tert*-butyl alkoxides are thought to react much faster to yield the kinetically trapped monoclinic polymorphs, whereas the primary and secondary alkoxides undergo a slower transformation to the tetragonal polymorph that has been predicted to be the thermodynamically more stable structure at dimensions <30 nm on the basis of surface energy considerations.[33] Notably, for the preparation of SiO_2, this nonhydrolytic sol−gel condensation approach works only for tertiary or benzylic carbons that are best able to stabilize carbocations.[34,35] Indeed, we have observed the formation of $CeO_{2-\delta}$ nanocrystals only for the condensation of cerium(IV) *tert*-butoxide with cerium halides. Figure 1A shows powder XRD patterns acquired for $CeO_{2-\delta}$ nanocrystals obtained by the condensation of cerium(IV) *tert*-butoxide with cerium(III) chloride, cerium(III) bromide, and cerium(III) iodide at 325 °C. Higher reaction temperatures do not appear to appreciably influence the size distribution or vacancy concentration of the obtained products. Consistent with the S_N1 nature of this reaction, the halide atom does not appear to make a significant difference to the reaction rate, and $CeO_{2-\delta}$ nanocrystals have been obtained for all the halides tested here with the tertiary alkoxide. A modified version of eq 2 can be written to account for the heterocondensation of Ce(III) and Ce(IV) species as per

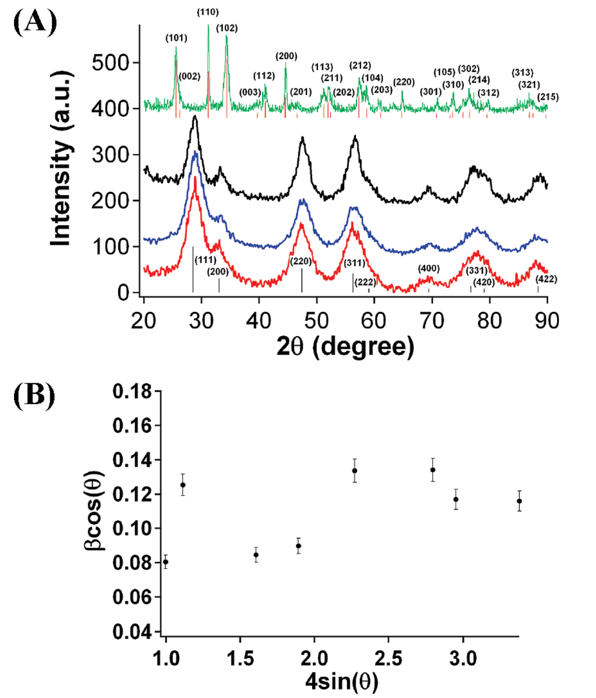

Figure 1. (A) XRD patterns of $CeO_{2-\delta}$ nanocrystals prepared by the condensation of Ce(IV) *tert*-butoxide with (from bottom to top) $CeCl_3$, $CeBr_3$, and CeI_3. The top pattern (green) corresponds to CeOCl nanocrystals prepared by the condensation of Ce(IV) isopropoxide with $CeCl_3$. (B) Williamson−Hall plot over an extended 2θ range for $CeO_{2-\delta}$ nanocrystals prepared from Ce(IV) *tert*-butoxide and $CeCl_3$.

$$4Ce^{3+}X_3 + 3Ce^{4+}(OR)_4 \rightarrow (Ce^{3+})_4(Ce^{4+})_3O_{12} + 12RX \tag{3}$$

In other words, the product nanocrystals are expected to be mixed valence in nature with a large concentration of oxygen vacancies. The XRD patterns for the nanocrystals obtained by the condensation of cerium(IV) *tert*-butoxide with cerium halides shown in Figure 1A can be indexed to the cubic fluorite structure of CeO_2 with $Fm\bar{3}m$ space group (Joint Committee on Powder Diffraction Standards (JCPDS) no. 34-0394), indicating the retention of this structure despite the high density of point defects. The fluorite structure can be conceptualized as a cubic close-packed array of cerium ions with the oxide ions occupying every tetrahedral hole. To maintain electroneutrality, the incorporation of a large concentration of Ce^{3+} species according to eq 3 requires the formation of a high concentration of oxygen vacancies. Notably, these are oxygen vacancies required by the stoichiometry of the reaction. Several studies have, additionally, indicated the spontaneous reduction of Ce^{4+} species in ultrasmall CeO_2 nanocrystals, often as part of a surface reconstruction process.[6,21,36,37] The TOPO used in the nonhydrolytic condensation reaction acts as both a solvent and a coordinating ligand for the growth of CeO_2 nanocrystals. The XRD patterns in Figure 1A show significant broadening arising from the small size of the particles. Figure 1B presents a Williamson—Hall plot to separate the contributions of size and strain to the broadening of the XRD reflections. Deconvolution of the contributions of size and strain is possible because they have different angular dependences:[37]

$$\beta_{\mathrm{Total}} = \beta_{\mathrm{size}} + \beta_{\mathrm{strain}} = \frac{0.9\lambda}{t\cos\theta} + \frac{4(\Delta d)\sin\theta}{d\cos\theta} \quad (4)$$

where β_{Total} is the full width at half-maximum of the XRD reflection, β_{size} is the contribution of finite size to the broadening of the reflection, β_{strain} is the contribution of strain to the broadening of the reflection, t is the crystal size, θ is the diffraction angle, λ is the wavelength of the incident X-rays, and Δd is the difference in the d spacing of a typical peak. A representative Williamson—Hall plot based on a diffraction pattern for $CeO_{2-\delta}$ nanocrystals acquired for 2θ values ranging from 20 to 120° is shown in Figure 1B. The absence of a clear slope in the plot suggests the absence of internal strain in these particles; the broadening of the diffraction peaks can, thus, be attributed primarily to the finite size of the particles. These results are consistent with the findings of Zhou and Huebner for CeO_2 nanocrystals grown using a batch reactor.[37] These authors have found significant strain in particles >5 nm in size but have noted that 3.9 and 4.3 nm diameter CeO_2 nanocrystals are largely free of internal strain. The $CeO_{2-\delta}$ nanocrystals grown by our nonhydrolytic approach have diameters <3 nm, and thus, it is not surprising that they are not significantly strained.

Figure 1A also illustrates that, upon substituting cerium(IV) *tert*-butoxide with a secondary cerium alkoxide, cerium(IV) isopropoxide, in the nonhydrolytic condensation reaction, $CeO_{2-\delta}$ nanocrystals are no longer obtained. Instead, we observe the formation of tetragonal CeOCl nanocrystals with the space group *P*4/*nmm* (JCPDS no. 81-0791) after reaction for 4 h. These observations are consistent with previous findings on the preparation of SiO_2 by nonhydrolytic condensation wherein only tertiary and benzylic carbons that are able to stabilize carbocations yield the desired oxide material.[34,35] The matlockite phase oxyhalide is formed because of a competing ligand-exchange reaction that yields cerium chloroalkoxides as per[30,38]

$$\mathrm{MCl}_n + \mathrm{M'(OR)}_n \rightarrow \mathrm{MCl}_{n-x}(\mathrm{OR})_x + \mathrm{M'Cl}_x(\mathrm{OR})_{n-x} \quad (5)$$

The chloroalkoxides can further condense to yield the CeOCl nanocrystals. Consistent with the slower reaction for the cerium isopropoxide, no solid products are obtained after 2 h. These observations, thus, clearly underline the influence of the alkyl chain in the metal alkoxide precursor in controlling the structure and composition of the obtained nanocrystalline products.[33]

TEM images of the obtained nanocrystals are shown in Figure 2. The particles have been deposited onto the TEM grid from a hexane solution. Figure 2A shows a low-resolution image of $CeO_{2-\delta}$ nanocrystals with excellent dispersion and hardly any evidence of the deleterious agglomeration observed for CeO_2 nanoparticles prepared by hydrolytic approaches. The excellent dispersion of the nanocrystals arises from the TOPO ligands on the nanocrystal surfaces that prevent agglomeration. The average particle size has been determined by measuring >50 particles for each sample using ImageJ image analysis software. The nanocrystals prepared using $CeCl_3$ are the smallest, with an average size of 1.5 nm, whereas the nanocrystals prepared using $CeBr_3$ and CeI_3 are slightly larger with average dimensions of 2.4 and 2.6 nm, respectively. Notably, this trend of increased size with decreasing nucleophilicity is opposite to the findings of Trentler et al. for TiO_2 nanocrystals.[29] These authors have postulated that metal halides can act as crystallization agents in this reaction; the lower valence of the cerium in the cerium halides, +3 as compared with +4 in $TiCl_4$, may account for the observed differences in the dependence of size on nucleophilicity. The tetragonal CeOCl nanocrystals derived from the Ce(IV) isopropoxide precursor are shown in Figure 2B and have an average size of 1.8 nm.

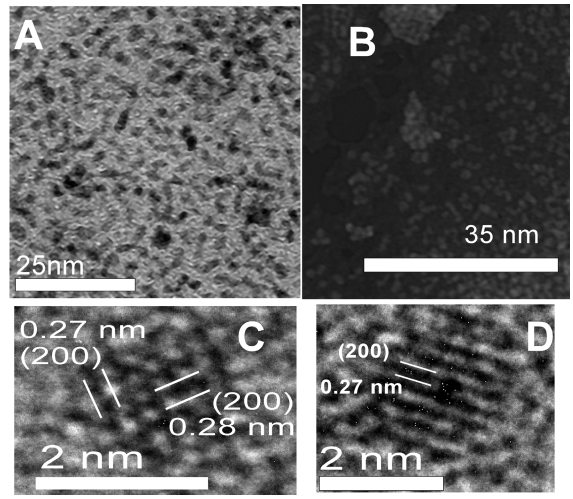

Figure 2. (A) Low-magnification image of $CeO_{2-\delta}$ nanoparticles with an average diameter of 1.5 nm synthesized from Ce(IV) *tert*-butoxide and $CeCl_3$. (B) Low-magnification image of CeOCl nanocrystals with an average diameter of 1.8 nm synthesized from Ce(III) isopropoxide and $CeCl_3$. Lattice-resolved images of a typical $CeO_{2-\delta}$ nanocrystal showing the {100} preferential surface terminating planes for nanocrystals synthesized by the condensation of Ce(IV) *tert*-butoxide with (C) $CeCl_3$ and (D) CeI_3.

Figure 2C,D shows representative lattice-resolved HRTEM images of $CeO_{2-\delta}$ nanocrystals synthesized by the condensation of $CeCl_3$ and CeI_3 with Ce(IV) *tert*-butoxide, respectively. The nanocrystals are observed to be single-crystalline, and both images show an interplanar separation of ~0.27 nm, corresponding to the separation between (200) planes. Surprisingly, the nanocrystals appear to be bound by {100} crystallographic facets, which represents a relatively high-energy terminating surface in CeO_2. Previous theoretical modeling of CeO_2 surfaces has shown that the ordering of surface energy follows (111) < (110) < (100).[39] The stabilization of the dipolar high-energy (100) terminating planes observed here likely originates from the strongly preferential binding of the TOPO ligands, which prevents the relaxation of the particle geometry to form equilibrium structures that would expose low-energy planes. Consistent with the low internal strain observed for these nanocrystals (Figure 1B), Si and Flytzani-Stephanopoulos have observed that CeO_2 nanocubes bound by (100) planes show lower internal strain as compared with that of nanostructures bound by (111) and (110) facets.[26] The termination of the nanocrystal surfaces with {100} planes is ideal for their use as

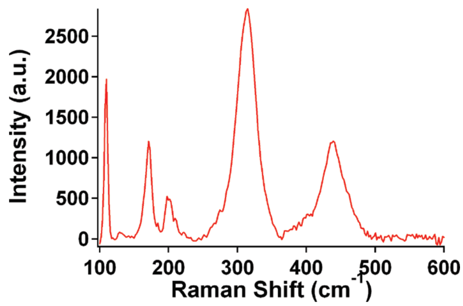

Figure 3. Raman spectrum of CeOCl nanocrystals prepared by the condensation of Ce(IV) isopropoxide with $CeCl_3$.

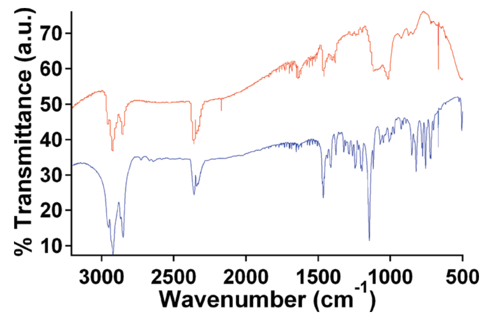

Figure 4. FTIR spectra of TOPO (bottom) and TOPO-capped $CeO_{2-\delta}$ nanocrystals (top).

CO oxidation catalysts. Lundberg et al. have shown that the exposure of {100} facets increases the reactivity of mesoporous CeO_2 toward CO oxidation.[40] Analogously, Mai et al. have shown very high CO oxidation activity for CeO_2 nanocubes bound by reactive {100} planes, derived primarily from the ease of oxygen vacancy formation on these planes and the availability of not only surface but also bulk lattice oxygens for CO conversion due to the facile migration of vacancies from the bulk to the surface.[19b]

Further structural characterization of the $CeO_{2-\delta}$ nanocrystals comes from Raman spectroscopy measurements. Figure S1 (Supporting Information) shows the Raman spectra of $CeO_{2-\delta}$ nanocrystals obtained using $CeCl_3$, $CeBr_3$, and CeI_3 as precursors. The spectra are characterized by a broad peak at $\sim$445–455 cm^{-1}, attributable to the triply degenerate F_{2g} lattice mode of cubic CeO_2. The spectra are strongly asymmetrically broadened due to phonon confinement and the presence of oxygen vacancies.[41] Consistent with the strong phonon confinement in these ultrasmall nanostructures, the F_{2g} lattice mode is shifted to lower wavenumbers for the 1.5 nm nanocrystals prepared using the $CeCl_3$ precursors as compared with those of the 2.4 and 2.6 nm nanocrystals prepared using $CeBr_3$ and CeI_3 as precursors. Figure 3 shows the Raman spectrum acquired for the CeOCl nanocrystals prepared by the condensation of Ce(IV) isopropoxide with cerium(III) chloride. A larger number of peaks are observed as compared with those of $CeO_{2-\delta}$, consistent with the lower tetragonal symmetry of the CeOCl lattice. On the basis of literature data and previous assignments for the structurally very similar matlockite LaOCl structure, the Raman mode at 188 cm^{-1} has A_{1g} symmetry, the modes at $\sim$122, 215, and 439 cm^{-1} have E_g symmetry, and the mode at 315 cm^{-1} can be assigned to phonons with A_{1g} or B_{2g} symmetry.[42,43] The broad line shapes and shifts of the E_g and B_{2g} peaks to lower wavenumbers compared with those of literature data are also likely a result of phonon confinement.

Figure 4 contrasts FTIR spectra acquired for the TOPO ligands and TOPO-capped $CeO_{2-\delta}$ nanocrystals prepared by the condensation of $CeCl_3$ and Ce(IV) *tert*-butoxide. A broad peak at $\sim$400 cm^{-1} is observed for the $CeO_{2-\delta}$ nanocrystals and can be attributed to Ce–O stretches. Remarkably, the P=O stretch observed at 1145 cm^{-1} in TOPO is split and shifted to two distinctive modes at 1100 and 1020 cm^{-1} in the $CeO_{2-\delta}$ nanocrystals, confirming the coordination of the TOPO ligands to Ce^{3+} and Ce^{4+} ions on the surfaces of $CeO_{2-\delta}$ nanocrystals. Coordination of the oxygen atom of TOPO to cerium ions weakens the P=O bond, shifting the P=O stretch to lower frequencies. The splitting of this peak suggests the existence of two different coordination modes, likely to Ce^{3+} and Ce^{4+} ions on the nanocrystal surface. The peaks observed around 2930 cm^{-1} correspond to C–H stretches from the alkyl chains on the TOPO ligands. The spectral features around 1460 cm^{-1} can be assigned to C–H bending modes, further corroborating the role of TOPO in passivating the surfaces of the $CeO_{2-\delta}$ nanocrystals. The nonhydrolytic condensation of cerium alkoxides and cerium halides has also been attempted in the presence of added phosphonic acid ligands, such as octylphosphonic acid and hexylphosphonic acid, using both 99% TOPO and 1-octadecene as solvents. However, the phosphonic acid ligands appear to more strongly bind cerium ions, and a mixture of cerium phosphates are obtained instead of $CeO_{2-\delta}$ nanocrystals. The relatively weaker binding of TOPO to Ce^{3+}/Ce^{4+} ions may, thus, facilitate nanocrystal growth by enabling facile monomer addition after nucleation.

Figure 5A shows a digital photograph of hexane solutions of $CeO_{2-\delta}$ nanocrystals prepared using different cerium halide precursors. The TOPO ligands impart solubility in nonpolar organic solvents, and no visible scattering due to particle agglomeration is observed even after 3 months. Figure 5B shows optical absorption spectra acquired for these hexane solutions. The colors of the nanocrystal solutions originate from their strong absorbance at <300 nm wavelengths, which, in turn, arises from the ligand-to-metal charge-transfer absorption involving the promotion of an electron from an oxygen 2p level to a cerium 4f level. This band overlaps with weaker $4f^1 \rightarrow 5d^1$ allowed transitions observed for Ce^{3+} ions at 6.3 eV. As discussed in further detail below, the $CeO_{2-\delta}$ nanocrystal samples prepared using $CeCl_3$, $CeBr_3$, and CeI_3 have very different Ce^{3+} ion concentrations.

The size-dependent blue-shifting of the absorption edge of CeO_2 nanocrystals has been extensively studied over the last several years and remains somewhat controversial.[6,13,14,23a] Based on the effective mass approximation, one possible origin of the observed blue shifts is the quantum confinement effect wherein the spatial confinement of the charge carriers leads to an increased optical band gap. Such a quantum confinement effect can also impart more direct character to optical transitions.[13,18a] In contrast, Tsunekawa et al. have attributed the blue-shifting of the absorption spectra as a function of size to a valence change of Ce^{4+} to Ce^{3+} ions in CeO_2 nanocrystals.[6] The direct and indirect band gaps of the prepared $CeO_{2-\delta}$ nanocrystals have been deduced from the optical absorption spectra shown in Figure 5B on the basis of determination of the absorption coefficient α according to

$$\alpha = \frac{2.303 \times 10^3 A\rho}{lc} \tag{6}$$

where A is the absorbance of the sample, ρ is the real density of CeO_2 (7.28 g/cm^3), l is the path length of the quartz cell, and c is the concentration of the $CeO_{2-\delta}$ nanocrystal solution. Figure 5C show plots of $(\alpha h\nu)^2$ versus photon energy, where

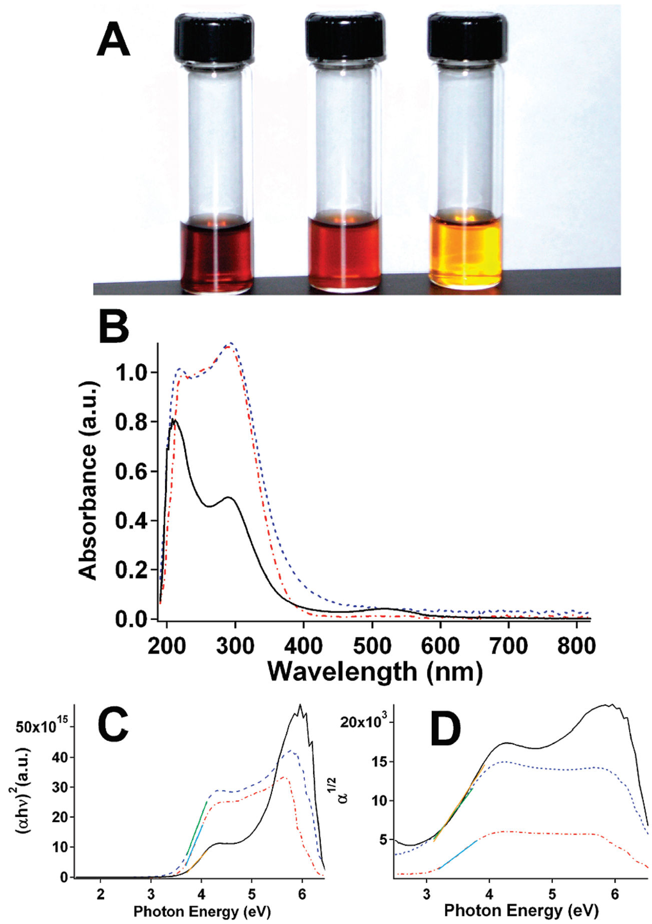

Figure 5. (A) Stable solutions of $CeO_{2-\delta}$ nanoparticles prepared by the condensation of Ce(IV) *tert*-butoxide and $CeCl_3$ (left), $CeBr_3$ (middle), and CeI_3 (right). (B) UV−vis absorption spectra of $CeO_{2-\delta}$ nanocrystals prepared by the condensation of Ce(IV) *tert*-butoxide and $CeCl_3$ (red), $CeBr_3$ (blue), and CeI_3 (black), showing strong absorption below 300 nm. (C) Plot of $(\alpha h\nu)^2$ versus photon energy for $CeO_{2-\delta}$ nanocrystals prepared by the condensation of Ce(IV) *tert*-butoxide and $CeCl_3$ (red), $CeBr_3$ (blue), and CeI_3 (black). Linear extrapolations used to calculate the direct band gaps are also shown. (D) Plot of $\alpha^{1/2}$ versus photon energy for $CeO_{2-\delta}$ nanocrystals prepared by the condensation of Ce(IV) *tert*-butoxide and $CeCl_3$ (red), $CeBr_3$ (blue), and CeI_3 (black). Linear extrapolations used to calculate the indirect band gaps are also shown.

$h\nu$ is the photon energy. For direct optical transitions, α varies with the photon energy as

$$\alpha \propto \frac{\sqrt{h\nu - E_d}}{h\nu} \tag{7}$$

where E_d is the band gap energy for direct transitions. Extrapolation of the linear regions of the plot enables determination of the direct band gap values. For $CeO_{2-\delta}$ nanocrystals prepared using $CeCl_3$, $CeBr_3$, and CeI_3 as precursors, the direct band gaps have been found to be 3.60, 3.55, and 3.67 eV, respectively (Figure 5C). These values are increased by 0.41, 0.36, and 0.48 eV, respectively, as compared with the literature value of 3.19 eV reported for bulk polycrystalline CeO_2, suggesting the presence of significant quantum confinement in these nanocrystals.[44] Zhang et al. have illustrated that direct band gap values for CeO_2 nanocrystals are strongly dependent not only on particle size but also on the preparation method because blue shifts induced by quantum confinement are counteracted

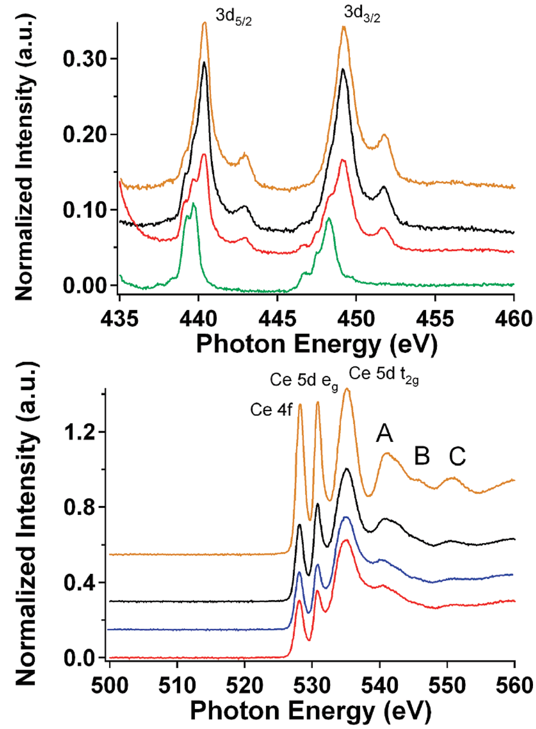

Figure 6. (A) NEXAFS spectra showing the second harmonic of the Ce M-edge (from top to bottom): bulk CeO_2 standard (brown), $CeO_{2-\delta}$ nanocrystals prepared using CeI_3 (black), $CeO_{2-\delta}$ nanocrystals prepared using $CeCl_3$ (red), and bulk $CeCl_3$ (green). (B) O K-edge NEXAFS spectra (from top to bottom): bulk CeO_2 standard (brown), $CeO_{2-\delta}$ nanocrystals prepared using CeI_3 (black), $CeO_{2-\delta}$ nanocrystals prepared using $CeBr_3$ (blue), and $CeO_{2-\delta}$ nanocrystals prepared using $CeCl_3$ (red).

by red shifts induced by dielectric confinement.[18] These authors have also noted little difference in the direct band gap values below a particle size of 4 nm. The differences in direct band gap values observed for the nanocrystals here, thus, likely originate from differences in surface states. Surface bands originating from different surface valences or exposed facets can contribute to long wavelength absorption, leading to the observed variability in the direct band gaps.[18]

For indirect transitions, α varies with photon energy as

$$\alpha \propto \frac{(h\nu + E_p - E_i)^2}{e^{h\nu/kT} - 1} + \frac{(h\nu - E_p - E_i)^2 e^{h\nu/kT}}{e^{h\nu/kT} - 1} \tag{8}$$

where E_i is the band gap energy for indirect transitions, E_p is the phonon energy, k is Boltzmann's constant, and T is the absolute temperature. Figure 5D shows plots of $\alpha^{1/2}$ versus photon energy. Again, on the basis of the extrapolation of linear regions of the plot, indirect band gaps of 2.98, 2.63, and 2.73 eV have been deduced for nanocrystals prepared using $CeCl_3$, $CeBr_3$, and CeI_3, respectively. These variations are, again, thought to arise from differences in surface states.

Further characterization of the electronic structure of the $CeO_{2-\delta}$ nanocrystals comes from NEXAFS spectroscopy measurements at Ce M- and O K-edges (Figure 6). NEXAFS spectroscopy is a powerful element-specific probe of the frontier orbital levels of transition-metal oxides because it involves the excitation of electrons from core levels to empty or partially filled states.[45,46] The peak positions and line shapes of NEXAFS resonances, thus, contain considerable information about the metal oxidation state, crystal field splitting, and the unoccupied density of states (DOS) above the Fermi level.[46,47] The Ce $M_{4,5}$-edge corresponds to electron transitions from Ce 3d core levels to 4f unoccupied electronic states above the Fermi level. Two distinctive features are expected because of spin orbit splitting, which gives rise to characteristic $3d_{3/2} \rightarrow 4f_{5/2}$ (M_4) and $3d_{5/2} \rightarrow 4f_{7/2}$ (M_5) spectral features. However, owing to the strong interaction of the photogenerated 3d core hole with 4f states, Ce $M_{4,5}$-edge spectra are dominated by multiplet effects and do not accurately reflect the atom-projected DOS in CeO_2.[48] In other words, the simple single-particle approximation is no longer valid for the Ce M-edge because of the strong overlap of the core wave function (arising from 3d holes) with the valence wave function (arising from 4f holes), which gives rise to distinctive vector-coupled final states.[49] However, atomic multiplet theory incorporating accurate core–hole spin orbit couplings and atomic Slater–Condon parameters allows for a reasonable description of the 3d NEXAFS spectra of rare earth oxides.[48,49] Figure 6A shows second harmonic Ce $M_{4,5}$-edge spectra measured for 1.5 and 2.6 nm diameter $CeO_{2-\delta}$ nanocrystals prepared using $CeCl_3$ and CeI_3 as the halide precursors. Second harmonic spectra have been acquired for improved energy resolution. These spectra are compared to Ce $M_{4,5}$-edge X-ray absorption spectra of two standard samples, a bulk CeO_2 sample (99.5% purity purchased from Alfa Aesar) that serves as a standard for Ce^{4+} absorption and a bulk $CeCl_3$ sample (99.5% purity, Aldrich) that serves as a standard for Ce^{3+} absorption. The bulk Ce^{4+} standard is characterized by M_5 and M_4 features around 440 and 449 eV, respectively, with weaker shoulders around 442 and 451 eV. In contrast, the bulk Ce^{3+} standard shows M_5 and M_4 peaks with considerably finer structure in the 439–440 eV (two overlapping features) and 446–448 eV (three overlapping features) regions, respectively. Kucheyev et al. have performed atomic multiplet calculations for Ce^{3+} and Ce^{4+} ions that are in good agreement with the spectral features observed here.[48] Consequently, the Ce $M_{4,5}$-edge spectra are an excellent probe of the valence of cerium ions (and, thus, the presence of oxygen vacancies) in the as-prepared $CeO_{2-\delta}$ nanocrystals. Figure 6A clearly illustrates that the Ce $M_{4,5}$-edge spectra for the 1.5 nm $CeO_{2-\delta}$ nanocrystal sample prepared using $CeCl_3$ as the halide precursor have a far greater contribution from Ce^{3+} species as compared with that of the 2.6 nm diameter $CeO_{2-\delta}$ nanocrystal sample prepared using CeI_3 as the halide precursor. However, the presence of a significant concentration of Ce^{3+} species is apparent even for the latter sample. On the basis of the relative ratios of the integrated intensities of the M_5 and M_4 features, the $CeO_{2-\delta}$ nanocrystals prepared using $CeCl_3$ are thought to have ~60% (±3%) of the cerium species as Ce^{3+} ions, whereas the nanocrystals prepared using CeI_3 have ~7% (±3%) of the cerium species as Ce^{3+} ions (assuming similar absorption cross sections for Ce^{3+} and Ce^{4+} ions). The significantly increased Ce^{3+} ion concentration in the smaller particles is consistent with previous measurements, suggesting that the Ce^{3+} concentration increases dramatically with a reduction in particle size.[6,21,36]

The O K-edge spectra correspond to transitions from 1s core levels to states with some 2p character. The covalent contribution to bonding in CeO_2 implies the strong hybridization of O 2p levels with Ce 4f and 5d states, and thus, the O K-edge spectra serve as an effective probe of the electronic structure of transition-metal oxides.[46,50] Two distinctive regions can be identified in the O K-edge spectra of the $CeO_{2-\delta}$ nanocrystals and bulk CeO_2 standard shown in Figure 6B. The first three spectral features are related to the electronic structure of the material, whereas the subsequent features labeled A, B, and C arise from multiple scattering from neighboring shells of atoms and are related to the geometric structure.[50] The first sharp resonance at around ~531 eV arises from transitions to O 2p states hybridized with Ce 4f levels; based on atom-projected DOS calculations, this band represents the lowest-lying level in the CeO_2 conduction band.[50,51] The O p projected DOS calculations show that the next two spectral features arise from the hybridization of the O 2p levels with the Ce 5d levels. The Ce 5d orbitals are split into e_g and t_{2g} peaks by crystal field splitting. These three spectral features have comparable intensities in the NEXAFS spectrum of the bulk CeO_2 standard with a very high predominance of Ce^{4+} ions. On comparison of these with the $CeO_{2-\delta}$ nanocrystals prepared using CeI_3, $CeBr_3$, and $CeCl_3$ as the cerium halide precursors, the Ce 4f and the e_g peaks are clearly decreased in intensity relative to the t_{2g} peak. This suggests that some of these lower-lying levels are no longer empty, consistent with the considerable Ce^{3+} and oxygen vacancy concentration present in the nanocrystals. Notably, the diminution of the first two spectral features is most apparent for the smallest 1.5 nm nanocrystals prepared using $CeCl_3$ as the precursor, which corroborates the higher Ce^{3+} concentration observed for this sample in Ce M-edge measurements.

The spectral features beyond 540 eV in CeO_2 have been reproduced using multiple scattering calculations and are thought to reflect the mean-range order in the material based on scattering from both oxygen atoms and the heavy Ce^{4+}/Ce^{3+} cations.[50] These features are observed to be significantly damped in the spectra acquired for the $CeO_{2-\delta}$ nanocrystals. This may be a result of the high concentration of oxygen vacancies (corresponding to missing next-nearest-neighbor atoms) and the absence of long-range order. In multiple scattering calculations performed by Wu et al., only a 125 atom cluster (and not any smaller clusters) comprising both Ce and O atoms was able to reproduce these spectral features, suggesting the importance of intermediate range order.[50] In our nanocrystals with diameters <3 nm, a significant number of atoms reside on or in proximity to the surfaces and, thus, it is reasonable that spectral features corresponding to long-range order are significantly attenuated in intensity.

The versatility of this nonhydrolytic sol–gel condensation approach is further demonstrated by the incorporation of La in the $CeO_{2-\delta}$ lattice to form solid-solution $Ce_xLa_{1-x}O_{2-\delta}$ nanocrystals. A part or the entire amount of the cerium halide precursor in eq 3 has been replaced by $LaCl_3$, while still maintaining a halide/alkoxide ratio of 1. The amount of the Ce *tert*-butoxide precursor is fixed at 2 mmol in all the reactions. Table 1 summarizes the products obtained for these heterocondensation reactions using different concentrations of $LaCl_3$. The elemental compositions of the solid-solution products have been determined using ICP-OES. XRD and Raman measurements indicate that, at the different concentrations of $LaCl_3$, the samples are phase-pure materials, either fluorite $Ce_xLa_{1-x}O_{2-\delta}$ or matlockite $Ce_xLa_{1-x}OCl$, and no fluorite/matlockite mixtures within detectable limits are obtained at any of these concentrations. Figure 7A shows XRD patterns for the solid-solution nanocrystals. The rates of condensation of La and Ce in the nonhydrolytic condensation reaction are not the same, and thus, the product nanocrystals do not have a La/Ce ratio equal to that of the starting materials. This is not surprising because previous studies of heterocondensation reactions yielding solid-solution twin oxide $Hf_xZr_{1-x}O_2$ nanocrystals have illustrated that Zr is incorporated in greater amounts upon starting with equimolar amounts of Zr and Hf precursors.[30,33] Notably, when 0.25 mmol of $CeCl_3$ is substituted with $LaCl_3$, $Ce_{0.94}La_{0.06}O_2$

TABLE 1: Precursor Concentrations along with Stoichiometry and Crystal Structure of the Products of the Nonhydrolytic Sol–Gel Heterocondensation Reaction between Metal Alkoxides and Metal Halides. The Table Illustrates the Effect of Increasing Lanthanum in the Reaction Mixture

alkoxides (mmol)	halides (mmol)	composition	structure and space group
2 Ce *tert*-butoxide	2 CeI_3	CeO_2	fluorite *Fm3m*
2 Ce *tert*-butoxide	2 $CeBr_3$	CeO_2	fluorite *Fm3m*
2 Ce *tert*-butoxide	2 $CeCl_3$	CeO_2	fluorite *Fm3m*
2 Ce *tert*-butoxide	1.75 $CeCl_3$ 0.25 $LaCl_3$	$Ce_{0.94}La_{0.06}O_2$	fluorite *Fm3m*
2 Ce *tert*-butoxide	0.25 $CeCl_3$ 1.75 $LaCl_3$	$Ce_{0.79}La_{0.21}O_2$	fluorite *Fm3m*
2 Ce *tert*-butoxide	2 $LaCl_3$	$Ce_{0.58}La_{0.42}OCl$	matlockite *P3/nmm*
2 La isopropoxide	2 $LaCl_3$	LaOCl	matlockite *P4/nmm*

nanocrystals are obtained, which still retain the cubic fluorite structure (Figure 7A,B). No evidence for the formation of La_2O_3 has been found from XRD or Raman measurements. The fluorite structure is also preserved for $Ce_{0.79}La_{0.21}O_2$ nanocrystals obtained by substituting 1.75 mmol of $CeCl_3$ with $LaCl_3$. When the concentration of the La precursor is further increased to 2 mmol, the fluorite structure is no longer stabilized and, instead, the ligand-exchange reaction depicted in eq 5 appears to be favored, resulting in the formation of solid-solution $Ce_{0.58}La_{0.42}$-OCl oxyhalide nanocrystals with the matlockite structure. Notably, the reaction of $LaCl_3$ and La isopropoxide yields LaOCl with this same matlockite structure (Table 1). The inset to Figure 7A shows a Raman spectrum of LaOCl, corroborating the stabilization of this phase.[43] The HRTEM images in Figure 7B show that, analogous to $CeO_{2-\delta}$ nanocrystals obtained without doping, the La-doped $CeO_{2-\delta}$ nanocrystals also have {100} terminating planes.

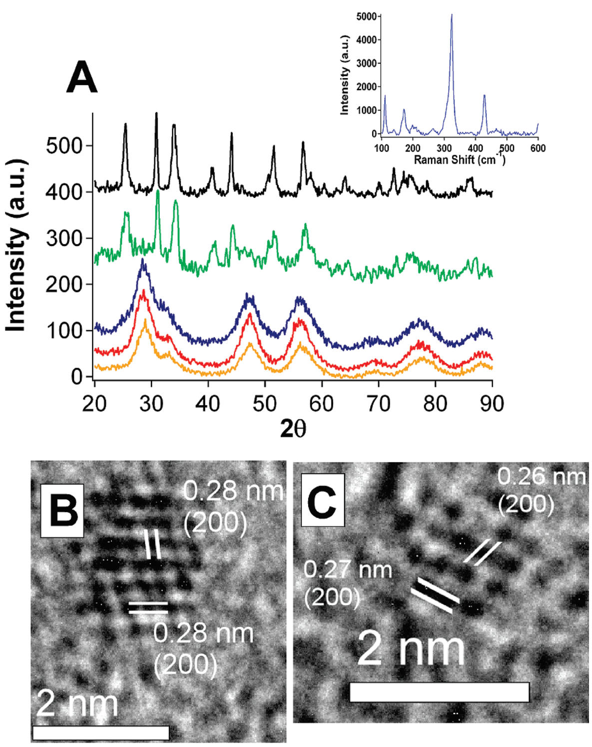

Figure 7. (A) XRD patterns showing the effect of increasing $LaCl_3$ concentration used during synthesis (from bottom to top): (i) 0 mmol of $LaCl_3$ + 2 mmol of $CeCl_3$ + 2 mmol of Ce(IV) *tert*-butoxide; (ii) 0.25 mmol of $LaCl_3$ + 1.75 mmol of $CeCl_3$ + 2 mmol of Ce(IV) *tert*-butoxide; (iii) 1.75 mmol of $LaCl_3$ + 0.25 mmol of $CeCl_3$ + 2 mmol of Ce(IV) *tert*-butoxide; (iv) 2 mmol of $LaCl_3$ + 0 mmol of $CeCl_3$ + 2 mmol of Ce(IV) *tert*-butoxide; (v) 2 mmol of $LaCl_3$ + 2 mmol of La(III) isopropoxide. The inset shows the Raman spectrum of LaOCl nanocrystals. (B) HRTEM image of a single $La_{0.06}Ce_{0.94}O_2$ nanocrystal retaining the cubic fluorite structure. (C) HRTEM image of a single $La_{0.21}Ce_{0.79}O_2$ nanocrystal retaining the cubic fluorite structure.

Conclusion

In conclusion, we demonstrate a novel nonhydrolytic approach based on the condensation of cerium halides with cerium alkoxides for the preparation of ligand-passivated $CeO_{2-\delta}$ and CeOCl nanocrystals soluble in nonpolar organic solvents. The alkoxide and halide precursors used in this versatile synthetic approach can be used to tune the composition and size of the obtained nanocrystals. Tertiary cerium alkoxides predominantly yield $CeO_{2-\delta}$ nanocrystals, whereas secondary cerium alkoxides yield CeOCl nanocrystals. The obtained nanocrystals are <3 nm in diameter and yield stable solutions in organic solvents because of the surface-coordinated TOPO ligands. In analogy with the multigram synthesis of well-defined ZrO_2 nanocrystals by nonhydrolytic condensation, it likely that this synthesis approach will be scalable to produce large quantities of ligand-passivated $CeO_{2-\delta}$ nanocrystals.[32] Optical absorption spectroscopy in combination with O K-edge and Ce M-edge NEXAFS studies provides insight into the electronic structure of the obtained nanocrystals. The synthesis process has also been extended to form solid-solution $Ce_xLa_{1-x}O_{2-\delta}$ nanocrystals that retain the cubic fluorite structure up to La concentrations of ~20%. The obtained solution-dispersible nanocrystals are ideal building blocks for inclusion within polymer nanocomposites for UV-shielding and flexible gate dielectric applications.

Acknowledgment. The authors gratefully acknowledge start-up funding from the University at Buffalo for support of this work. This work was partially supported by a seed grant from the Office of the Vice President of Research at the University at Buffalo. Dr. Yueling Qin is thanked for his assistance with TEM imaging. Certain commercial names are presented in this manuscript for purposes of illustration and do not constitute an endorsement by the National Institute of Standards and Technology.

Supporting Information Available: Raman spectra showing the triply degenerate F_{2g} lattice mode of cubic $CeO_{2-\delta}$ nanocrystals. This material is available free of charge via the Internet at http://pubs.acs.org.

References and Notes

(1) Law, M.; Goldberger, J.; Yang, P. *Annu. Rev. Mater. Res.* **2004**, *34*, 83.
(2) Murray, C. B.; Kagan, C. R.; Bawendi, M. G. *Annu. Rev. Mater. Sci.* **2000**, *30*, 546.
(3) Peng, Z. A.; Peng, X. *J. Am. Chem. Soc.* **2002**, *1\24*, 3343.
(4) Peng, X. *Adv. Mater.* **2003**, *15*, 459.
(5) Schermanz, K. In *Catalysis by Ceria and Related Materials*; Troverالli, A., Ed.; World Scientific: London, 2002.
(6) Tsunekawa, S.; Fukuda, T.; Kasuya, A. *J. Appl. Phys.* **2000**, *87*, 1318.
(7) Steele, B. C. H. *Solid State Ionics* **1984**, *12*, 391.
(8) Mogensen, M.; Sammes, N. M.; Tompsett, G. A. *Solid State Ionics* **2000**, *129*, 63.
(9) Schwab, R. G.; Steiner, R. A.; Mages, G.; Beie, H. J. *Thin Solid Films* **1992**, *207*, 288.
(10) Sabia, R.; Stevens, H. J. *Mach. Sci. Technol.* **2000**, *4*, 235.

(11) Frangoul, A. G.; Sundaram, K. B.; Wahid, P. F. *J. Vac. Sci. Technol., B* **1991**, *9*, 181.

(12) Nie, J. C.; Yamasaki, H.; Nakagawa, Y.; Develos-Bagarinao, K.; Murugesan, M.; Obara, H.; Mawatari, Y. *Appl. Phys. Lett.* **2005**, *86*, 192507/1.

(13) Nie, J. C.; Zhen, Y. H.; Dou, R. F.; Tu, Q. Y. *J. Appl. Phys.* **2008**, *103*, 054308/1.

(14) Hernandez-Alonso, M. D.; Hungria, A. B.; Martinez-Arias, A.; Coronado, J. M.; Conesa, J. C.; Soria, J.; Fernandez-Garcia, M. *Phys. Chem. Chem. Phys.* **2004**, *6*, 3524.

(15) Carrettin, S.; Concepcion, P.; Corma, A.; Lopez Nieto, J. M.; Puntes, V. M. *Angew. Chem., Int. Ed.* **2004**, *43*, 2538.

(16) Fu, Q.; Saltsburg, H.; Flytzani-Stephanopoulos, M. *Science* **2003**, *301*, 935.

(17) Hashmi, A. S. K.; Hutchings, G. J. *Angew. Chem., Int. Ed.* **2006**, *45*, 7896.

(18) (a) Zhang, Y.-W.; Si, R.; Liao, C.-S.; Yan, C.-H.; Xiao, C.-X.; Kou, Y. *J. Phys. Chem. B* **2003**, *107*, 10159. (b) Yang, S.; Gao, L. *J. Am. Chem. Soc.* **2006**, *128*, 9330–9331. (c) Han, W. Q.; Wu, L.; Zhou, Y. *J. Am. Chem. Soc.* **2005**, *127*, 12814–12815. (d) Vantomme, A.; Yuan, Z.-Y.; Du, G.; Su, B.-L. *Langmuir* **2005**, *21*, 1132–1135.

(19) (a) Zhou, H.-P.; Zhang, Y.-W.; Si, R.; Zhang, L.-S.; Song, W.-G.; Yan, C.-H. *J. Phys. Chem. C* **2008**, *112*, 20366–20374. (b) Mai, H.-X.; Sun, L.-D.; Zhang, Y.-W.; Si, R.; Feng, W.; Zhang, H.-P.; Liu, H.-C.; Yan, C.-H. *J. Phys. Chem. B* **2005**, *109*, 24380.

(20) Yin, L. X.; Wang, Y. Q.; Pang, G. S.; Koltypin, Y.; Gedanken, A. *J. Colloid Interface Sci.* **2002**, *246*, 78.

(21) Zhang, F.; Chan, S.-W.; Spanier, J. E.; Apak, E.; Jin, Q.; Robinson, R. D.; Herman, I. P. *Appl. Phys. Lett.* **2002**, *80*, 3283.

(22) Deshpande, A. S.; Pinna, N.; Beato, P.; Antonietti, M.; Niederberger, M. *Chem. Mater.* **2004**, *16*, 2599.

(23) (a) Maensiri, S.; Masingboon, C.; Laokul, P.; Jareonboon, W.; Promarak, V.; Anderson, P. L.; Seraphin, S. *Cryst. Growth Des.* **2007**, *7*, 950. (b) Li, X.; Li, J.-G.; Huo, D.; Xiu, Z.; Sun, X. *J. Phys. Chem. C* **2009**, *113*, 1806–1811.

(24) Si, R.; Zhang, Y.-W.; You, L.-P.; Yan, C.-H. *Angew. Chem., Int. Ed.* **2005**, *44*, 3256.

(25) Gu, H.; Soucek, M. D. *Chem. Mater.* **2007**, *19*, 1103.

(26) Si, R.; Flytzani-Stephanopoulos, M. *Angew. Chem., Int. Ed.* **2008**, *47*, 2884.

(27) Yu, W. W.; Chang, E.; Falkner, J. C.; Zhang, J.; Al-Somali, A. M.; Sayes, C. M.; Johns, J.; Drezek, R.; Colvin, V. *J. Am. Chem. Soc.* **2007**, *129*, 2871.

(28) Yin, M.; O'Brien, S. *J. Am. Chem. Soc.* **2003**, 125.

(29) Trentler, T. J.; Denler, T. E.; Bertone, J. F.; Agrawal, A.; Colvin, V. L. *J. Am. Chem. Soc.* **1999**, *121*, 1613.

(30) Tang, J.; Fabbri, J.; Robinson, R. D.; Zhu, Y.; Herman, I. P.; Steigerwald, M. L.; Brus, L. E. *Chem. Mater.* **2004**, *16*, 1336.

(31) Tang, J.; Zhang, F.; Zoogman, P.; Fabbri, J.; Chan, S.-W.; Zhu, Y.; Brus, L. E.; Steigerwald, M. L. *Adv. Funct. Mater.* **2005**, *15*, 1595.

(32) Joo, J.; Yu, T.; Woon Kim, Y.; Min Park, H.; Wu, F.; Zhang, J. Z.; Hyeon, T. *J. Am. Chem. Soc.* **2003**, *125*, 6553.

(33) Depner, S. W.; Kort, K. R.; Banerjee, S. *CrystEngComm.* **2008**, *11*, 841–846.

(34) Vioux, A. *Chem. Mater.* **1997**, *9*, 2292.

(35) Corriu, R. J. P.; Leclercq, D.; Mutin, P. H.; Samson, H.; Vioux, A. *J. Organomet. Chem.* **1994**, *466*, 43.

(36) Wu, L.; Wiesmann, H. J.; Moodenbaugh, A. R.; Klie, R. F.; Zhu, Y.; Welch, D. O.; Suenaga, M. *Phys. Rev. B* **2004**, *69*, 125415/1.

(37) Zhou, X.-D.; Huebner, W. *Appl. Phys. Lett.* **2001**, *79*, 3512.

(38) Andrianainarivelo, M.; Corriu, R. J. P.; Leclercq, D.; Mutin, P. H.; Vioux, A. *J. Mater. Chem.* **1997**, *7*, 279.

(39) Sayle, T. X. T.; Parker, S. C.; Catlow, C. R. A. *Surf. Sci.* **1994**, *316*, 329.

(40) Lundberg, M.; Skarman, B.; Wallenberg, R. L. *Microporous Mesoporous Mater.* **2004**, *69*, 187.

(41) Spanier, J. E.; Zhang, F.; Robinson, R. D.; Chan, S.-W.; Herman, I. P. *Phys. Rev. B* **2001**, *64*, 245407/1.

(42) Del Cul, G. D.; Nave, S. E.; Begun, G. M.; Peterson, J. R. *J. Raman Spectrosc.* **1992**, *23*, 267.

(43) Weckhuysen, B. M.; Rosynek, M. P.; Lunsford, J. H. *Phys. Chem. Chem. Phys.* **1999**, *1*, 3157.

(44) Crnjak, O. Z.; Orel, B. *Phys. Status Solidi B* **1994**, *186*, K33.

(45) Stohr, J. *NEXAFS Spectroscopy*; Springer: Berlin, 1992.

(46) de Groot, F. M. F.; Grioni, M.; Fuggle, J. C.; Ghijsen, J.; Sawatzky, G. A.; Peterson, H. *Phys. Rev. B* **1989**, *40*, 5715.

(47) Chen, J. G. *Surf. Sci. Rep.* **1997**, *30*, 1.

(48) Kucheyev, S. O.; Clapsaddle, B. J.; Wang, Y. M.; van Buuren, T.; Hamza, A. V. *Phys. Rev. B* **2007**, *76*, 235420/1.

(49) de Groot, F. *Coord. Chem. Rev.* **2005**, *249*, 31.

(50) Wu, Z. Y.; Jollet, F.; Gota, S.; Thromat, N.; Gautier-Soyer, M.; Petit, T. *J. Phys.: Condens. Matter* **1999**, *11*, 7185.

(51) Rodriguez, J. A.; Hanson, J. C.; Kim, J.-Y.; Liu, G.; Iglesias-Juez, A.; Fernandez-Garcia, M. *J. Phys. Chem. B* **2003**, *107*, 3535.

JP903216B